Near-wall grid adaptation for wall-functions

Th. Alrutz, T. Knopp

Institute of Aerodynamics and Flow Technology
DLR (German Aerospace Center)
Bunsenstr. 10, 37073 Göttingen, Germany
Thomas.Alrutz@dlr.de

1. Introduction

The numerical solution of the Reynolds averaged Navier-Stokes (RANS) equations for aerodynamic flows requires a suitable resolution of boundary layers. The currently most popular turbulence models for such flows are of Spalart-Allmaras and of k-ω type [4], [5]. For these models, at the wall the no-slip condition is imposed for velocity and the accurate numerical resolution of both attached and separated boundary layers requires a so-called *low-Reynolds grid* with $y^+(1) \approx 1$ where $y(1)$ is the distance of the first node above the wall, v_t is the wall-parallel component of velocity, and $y^+(1)$ is defined by

$$y^+(1) \equiv \frac{y(1)u_\tau}{\nu}\ , \quad \text{where} \quad u_\tau = \sqrt{\nu \frac{\partial v_t}{\partial n}}\ , \qquad \nu = \frac{\mu}{\rho} \tag{1}$$

with density ρ, viscosityμ, outer normal $\vec{n}$ and so-called friction velocity u_τ.
The condition $y^+(1) \approx 1$ has to be ensured during grid-generation by specifying the first spacing $y(1)$ and using an estimate for u_τ, e.g., from a semi-empirical relation for a flat-plate turbulent boundary layer. However, there are regions in complex geometries where the grid-generator cannot reach the specified $y(1)$-value. Moreover, the semi-empirical guess for u_τ may deviate from the value for u_τ from the RANS solution in regions of complex flow. As a remedy, the DLR TAU-code provides a grid-adaptation module, which allows to ensure a user-defined target value for $y^+(1)$ based on the underlying RANS solution. This method will be referred to as y^+-adaptation.
In the present paper, this y^+-adaptation technique is employed as part of a grid and flow adaptive universal wall-function method [2]. Wall-functions are still strongly relevant in CFD as they allow for a significant reduction of the grid size and a noticeable acceleration of the nonlinear solver. The wall-function method prescribes the wall-shear stress and no-penetration at the wall. In the noval approach [1], the wall-shear stress is computed from the wall-parallel velocity at $y(1)$ by assuming that the solution between $y = 0$ and $y(1)$ is given by the turbulence-model specific solution of a flat-plate turbulent boundary layer at zero pressure gradient. Such walls functions allow for solutions independent of the wall-normal spacing $y(1)$ for flows close to equilibrium, e.g., fully developed turbulent boundary layer flows [1]. However, aerodynamic flows are characterised by *(i)* stagnation points and subsequent laminar resp. not fully developed turbulent flow, *(ii)* regions of significant pressure gradient parameter due to a strong (adverse) pressure gradient at a typically moderate Reynolds number and *(iii)* regions of separation and reattachment. These flow situations are very important not only for flows around airfoils and rotor blades, but even more for complex aircraft configurations with flaps, engines etc. In these critical flow situations *(i)*-*(iii)* local mispredictions using wall functions may occur, which may cause large deviations in integral coefficients of engineering interest as lift, moment and drag.
As a remedy, the present paper proposes a near-wall grid adaptation technique to ensure a locally appropriate resolution depending on both the near-wall flow physics to be captured and the range of validity of the wall-function model. Critical regions are characterised by non-equilibrium flow situations which are detected by a flow based sensor. The near-wall grid adaptation is then made possible due to the hybrid character of the wall-function method, e.g., $y(1)$ can be shifted in the very near wall region without

introducing an error stemming from an inconsistent coupling of turbulence models. We note that in classical wall-function methods, such an error is present due to the coupling of different turbulence models, i.e., a one- resp. two equation model for the global flow and an ad-hoc patched algebraic model for the near-wall region.

2. y^+-adaptation in the DLR TAU-code

The new wall-function approach is applied to the DLR TAU-Code [6]. Due to the dual mesh approach, the TAU-code supports hybrid grids, which may be composed of tetrahedra, prisms, hexahedra and/or pyramids. In the near-wall region, this allows to use anisotropic regular meshes consisting of hexahedra and/or prisms with a high aspect ratio whose edges are aligned with the wall-normal and wall-parallel directions. These are fitted to boundary layer flows, i.e., with a relatively large spacing in streamwise and spanwise direction but with a fine spacing in wall-normal direction with a suitable stretching factor to resolve the steep wall-normal gradients of the solution.

2..1. y^+-adaptation for low-Re grids

An accurate integration of the RANS equations down to the wall requires a so-called *low-Reynolds grid* with $y^+(1) = y(1)u_\tau/\nu \approx 1$ for all first nodes above the wall. In 3D flows, friction velocity u_τ may be computed from the vorticity tensor $\Omega(\vec{u})$ by

$$u_\tau = \sqrt{\frac{\mu}{\rho}|\Omega|}\,, \qquad \text{where} \quad |\Omega| = \sqrt{2\Omega(\vec{u}):\Omega(\vec{u})}\,, \quad \Omega(\vec{u}) = \frac{1}{2}\left(\vec{\nabla}\vec{u} - (\vec{\nabla}\vec{u})^T\right) \tag{2}$$

with the notation $A : B = \sum_{i,j=1}^{d} A_{ij}B_{ij}$ for two tensors A, B, with space dimension $d = 2, 3$. For complex flow problems, the low-Re grid condition can be satisfied only by using an adaptation of the near-wall grid w.r.t. $y^+(1)$. We assume a given surface discretization composed of triangles and/or quadrilaterals. Inside the regular near-wall layer, the nodes are located on (almost) wall-normal rays starting at the corresponding wall node. We use the following notation:

- $\vec{x}_{\mathrm{wp}}$: Surface (wall) node,
- $\vec{x}_{\mathrm{np}}$: First node above the wall corresponding to node wp,
- $\{\vec{x}_{\mathrm{wp}} + \lambda_p\vec{r}\}$: Ray of points starting at wall node $\vec{x}_{\mathrm{wp}}$ and ending at the outer edge of the regular layer; $\{\vec{x}_{\mathrm{wp}} + \lambda_p\vec{r}\} \equiv \{\, \vec{x} \in \mathbb{R}^d \mid \vec{x} = \vec{x}_{\mathrm{wp}} + \lambda_p\vec{r}\,,\ \ 0 \le p \le p_{\max}\}$ where the direction vector $\vec{r}$ may be non-constant.

Moreover we assume that $\vec{x}_{\mathrm{np}} - \vec{x}_{\mathrm{wp}}$ is almost parallel to the surface normal vector $\vec{n}$. Then the algorithm for y^+-adaptation with $y^+_{\mathrm{target}} = 1$ reads as follows.

1. Read RANS solution and grid.
2. y^+ grid adaptation.
   (a) For each surface node $\vec{x}_{\mathrm{wp}}$ do:
      i. Determine $\vec{x}_{\mathrm{np}}$ and compute u_τ from vorticity using equation (2).
      ii. From $y_{\mathrm{np}} = |\vec{x}_{\mathrm{np}} - \vec{x}_{\mathrm{wp}}|$ determine the $y^+_{\mathrm{np}} = y_{\mathrm{np}}u_\tau/\nu$.
      iii. Set $y_{\mathrm{new}} = y_{\mathrm{np}}\, y^+_{\mathrm{target}}/y^+_{\mathrm{np}}$.
   (b) Smooth the y_{new}-distribution.
   (c) For each surface node redistribute the points on its ray $\{\vec{x}_{\mathrm{wp}} + \lambda_p\vec{r}\}$ where the last point $\{\vec{x}_{\mathrm{wp}} + \lambda_{p,\max}\vec{r}\}$ remaines unchanged.
3. Interpolate RANS solution from old grid to new grid.

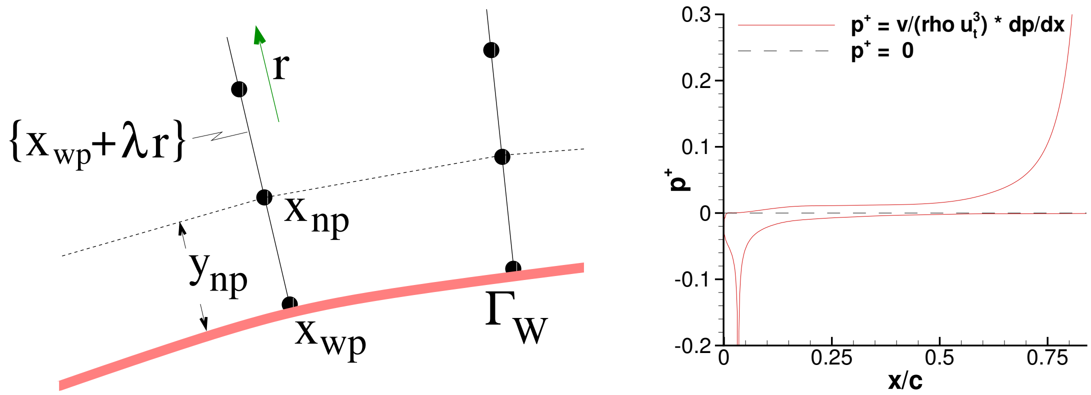

Figure 1: Left: Illustration of near-wall grid adaptation w.r.t. y^+. Right: Pressure gradient parameter p^+ for subsonic highlift A-airfoil.

Smoothing of the y_{new}-distribution is performed as follows. Denote K the number of smoothing steps, $y^i_{\text{np}} = y_{\text{new}}$ of node $\vec{x}^i_{\text{np}}$ after (2(a)iii), $\mathcal{N}(i)$ the set of indices of neighbour (adjacent) surface nodes of node i and $\#\mathcal{N}(i)$ their number. Then in smoothing step k

$$y^{i,k}_{\text{np}} = (1-\epsilon)\, y^{i,k-1}_{\text{np}} + \epsilon\, y^{\text{nei},k-1}_{\text{np}} \;\text{ with }\; y^{\text{nei},k-1}_{\text{np}} = \frac{1}{\#\mathcal{N}(i)} \sum_{j\in\mathcal{N}(i)} y^{j,k-1}_{\text{np}}.$$

Figures 2-3 demonstrate the y^+-adaptation for complex wing-body configurations.

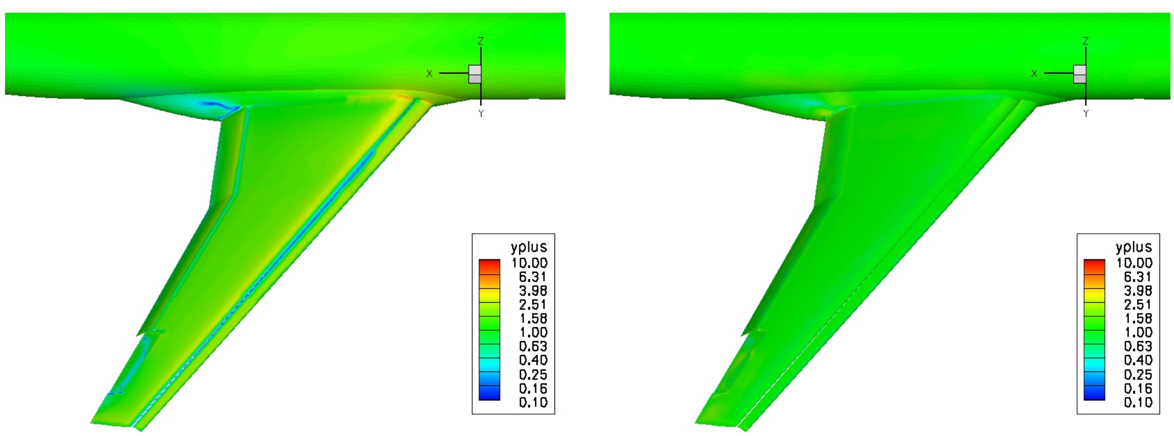

Figure 2: Eurolift highlift configuration wing-body with slats and flaps ($Re = 25 \times 10^6$, $Ma = 0.2$, $\alpha = 19°$): y^+-distribution without y^+-adaptation (left) and with adaptation (right).

2..2. Near-wall grid adaption for wall functions using a flow based sensor

In this section we describe the near-wall grid adaption for wall-functions using a flow based sensor. In aerodynamic flows, the following flow situations are beyond the range of validity of universal wall functions in the sense that relatively large deviations from the low-Re solution may occur if $y^+(1)$ is too large, viz., *(i)* stagnation points and subsequent not fully developed turbulent flow, *(ii)* regions of strong adverse pressure gradient ($p^+ > 0.1$), and *(iii)* regions of separated flow. As a remedy, a *near-wall grid adaptation* is employed, motivated by the fairly grid-independent results for $y^+(1) \lessapprox 10$ even in regions of complex flow, see also [1], [2].
On grids with $y^+(1) > 4$, relation (2) ceases to be valid. Then u_τ is estimated from the following

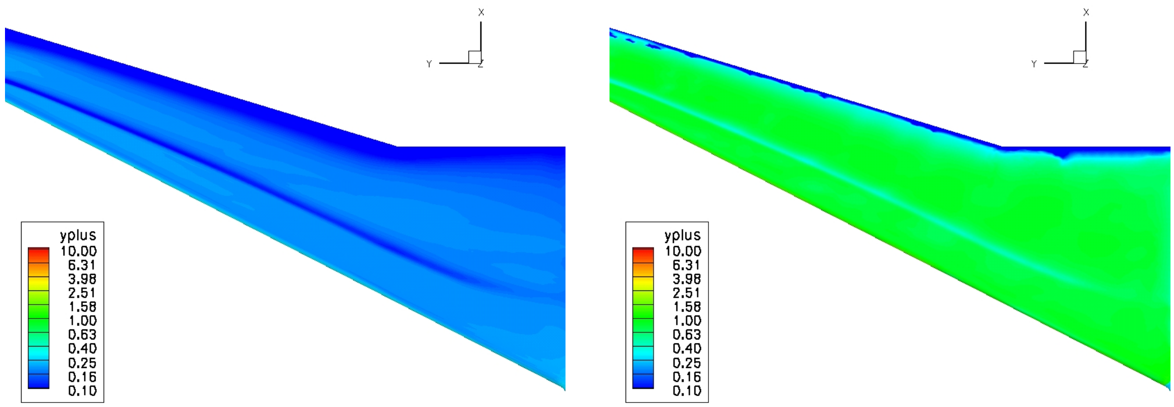

Figure 3: A-320 wing-body ($Re = 6.5 \times 10^6$, $Ma = 0.75$, $\alpha = 2.8°$): y^+-distribution without y^+-adaptation (left) and with adaptation (right).

nonlinear equation, known as the law of the wall by Reichardt, to be solved using Newton's method

$$u^+(1) = \mathrm{F}_{\mathrm{Rei}}(y^+(1)) \,, \qquad \mathrm{F}_{\mathrm{Rei}}(y^+) \equiv \frac{\ln(1+0.4y^+)}{\kappa} + 7.8\left(1 - e^{-\frac{y^+}{11.0}} - \frac{y^+}{11.0}e^{-\frac{y^+}{3.0}}\right) \tag{3}$$

with $u^+(1) = u(1)/u_\tau$, $y^+(1) = y(1)u_\tau/\nu$, $\kappa = 0.41$ and $u(1)$ being the wall-parallel velocity at $y(1)$, and $\kappa = 0.41$.

Regions of complex flow situations are detected by a flow based sensor. Both critical regions *(i)* and *(ii)* can be detected using the pressure gradient parameter p^+ as indicator

$$p^+ = \frac{\nu}{\rho u_\tau^3}\frac{\mathrm{d}p}{\mathrm{d}x} \tag{4}$$

which is computed from the streamwise pressure gradient $\mathrm{d}p/\mathrm{d}x$. As stagnation point and separation point are approached, $u_\tau \to 0$ and thus $p^+ \to \pm\infty$. Figure 1 shows p^+ vs. x/c with streamwise coordinate x and chord length c for the A-airfoil at subsonic highlift conditions ($Ma = 0.15$, $Re = 2.0 \times 10^6$, $\alpha = 13.3°$). Non-small values $p^+ > 0.02$ can be observed for $x/c > 0.5$ on the upper side of the airfoil, which is due to the relatively small Reynolds-number. Such non-small p^+-values in adverse pressure gradient flow (i.e., $\mathrm{d}p/\mathrm{d}x > 0$) cause a significant departure from the universal wall-law for large y^+ (see [2]).

Then in the algorithm for y^+-adaptation, step (2a) is modified as follows if wall-functions are used.

(a) For each surface node $\vec{x}_{\mathrm{wp}}$ do:

  i. Determine $\vec{x}_{\mathrm{np}}$ and compute u_τ using (3). Then set $y_{\mathrm{np}} = |\vec{x}_{\mathrm{np}} - \vec{x}_{\mathrm{wp}}|$ and determine $y^+_{\mathrm{np}} = y_{\mathrm{np}}u_\tau/\nu$.

  ii. Determine p^+ from (4) and check if $|p^+| > p^+_0$ for a given threshold value p^+_0.

  iii. Check if $\vec{x}_{\mathrm{wp}}$ is located in a region of strong surface curvature with flow stagnation.

  iv. Check if point $\vec{x}_{\mathrm{wp}}$ resides in a region of recirculating (separated) flow.

  v. Based on ii.-iv. set target value y^+_{target}.

  vi If $y^+_{\mathrm{target}} < y^+_{\mathrm{np}}$ then set $y_{\mathrm{new}} = y_{\mathrm{np}}\; y^+_{\mathrm{target}}/y^+_{\mathrm{np}}$, else $y_{\mathrm{new}} = y_{\mathrm{np}}$.

Some technical details are described in the following. Calculating u_τ using (3) is sufficient for the adaptation. We use the threshold value $p^+_0 = 0.09$ for indicating regions of strong pressure gradient. Regarding the leading edge region, p^+ is used as an indicator, and we note that $p^+ > 0$ as $\mathrm{d}p/\mathrm{d}x > 0$ for accelerated flow. As an additional indicator the surface curvature may be used, see e.g. [11] for

computational techniques. For 2D flows, regions of separated flow can be detected by the condition of recirculating flow $\vec{u}_\infty \cdot \vec{u}_{\text{np}} < 0$, where $\vec{u}_\infty$ and $\vec{u}_{\text{np}}$ denote the farfield velocity and the velocity at node $\vec{x}_{\text{np}}$ resp. In 3D flows in complex geometries, detection of separated flow is more complicated. Albeit, the separation point is still indicated by large p^+-values.
Concerning the target value for y^+, numerical tests suggest $y^+_{\text{target}} \in [5, 10]$ in regions of flow stagnation and not-fully developed turbulent flow and for strong adverse pressure gradient before separation, and $y^+_{\text{target}} \in [1, 5]$ in regions of separated flow.

3. Application to aerodynamic flow problems

In this section we apply the method to the transonic flow around the RAE2822 airfoil (at $Ma = 0.75$, $Re = 6.2 \times 10^6$, and $\alpha = 2.8°$ with shock induced separation), and to the A-airfoil at subsonic highlift conditions ($Ma = 0.15$, $Re = 2.0 \times 10^6$, $\alpha = 13.3°$). Calculations are performed on a series of O-type grids of hybrid type. The boundary layer is fully contained in the regular prismatic grid. In wall-normal direction a geometrical point distribution is used. We use grids with different spacing of the first node above the wall and a different number of nodes in the structured layer such that the thickness of the prismatic layer remains almost constant.

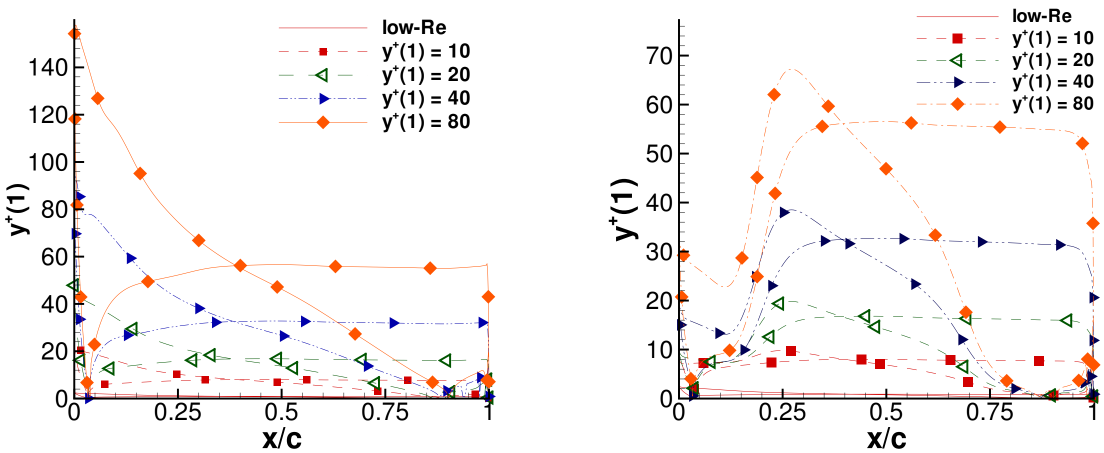

Figure 4: A-airfoil: $y^+(1)$ distribution without (left) and after adaptation (right).

For the A-airfoil we use $\epsilon = 0.6$ and $K = 200$. Figure 4 shows the y^+-distribution before and after adaptation. Figure 5 (left) shows a zoom of the c_p distribution at the leading edge for the SST k-ω model. The table in Figure 5 (right) gives the streamwise position of the separation point x_{sep} where c denotes the chord length. Values without brackets are obtained without adaptation. The improvement using adaptation (values in brackets) is discernible. The spreading in the separation point for each model is less than 1% but the predictions between the two turbulence models differ by 11%. Figure 6 shows that the grid-independence of the prediction for skin friction c_{f} is remarkable.
Secondly we apply the approach to the RAE 2822 case 10. We are interested in an improved grid-independence of the results close to the the leading edge and in the aft-shock separation region. Figure 7 shows the distribution of $y^+(1)$ for the SST k-ω model without (left) and with (right) y^+-adaptation. As intended, the wall-normal grid is shifted towards the low-Re regime in the vicinity of the leading edge, close to the shock and in the separation region. Figure 8 (left, without adaptation) shows a detail view of c_p in the leading edge region, predicted by the SA-Edwards model. The improvement with grid-adaptation (right) can be clearly seen. As shown in Figure 9, the grid-independence in c_f, in particular in the recirculation region, can also be increased significantly. Figure 10 shows that even for flow-details like Mach-number contours and streamtraces of velocity, there is close agreement between the wall-resolved RANS solution and the solution with wall-functions.

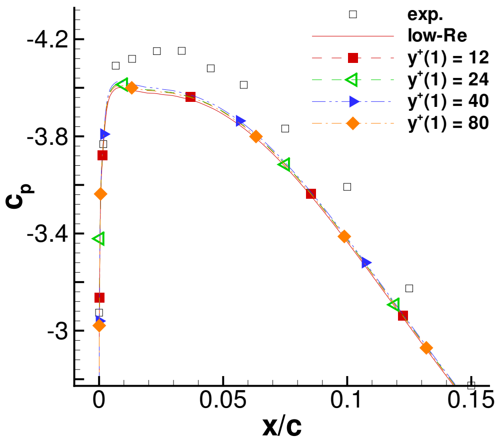

$y^+(1)$	N_y	x_{sep}/c SA-E	x_{sep}/c SST k-ω
low-Re	33	0.771	0.866
1	33	0.770	0.866
4	28	0.755	0.863
7	26	0.759	0.868
12	24	0.761	0.861
24	21	0.787	0.861 (0.864)
50	19	(0.771)	0.881 (0.873)
70	17	(0.788)	0.903 (0.867)

Figure 5: A-airfoil: Detail of c_{p} for SST k-ω model on adapted grid (left). Right: Prediction of separation point without adaptation and with adaptation (value in brackets).

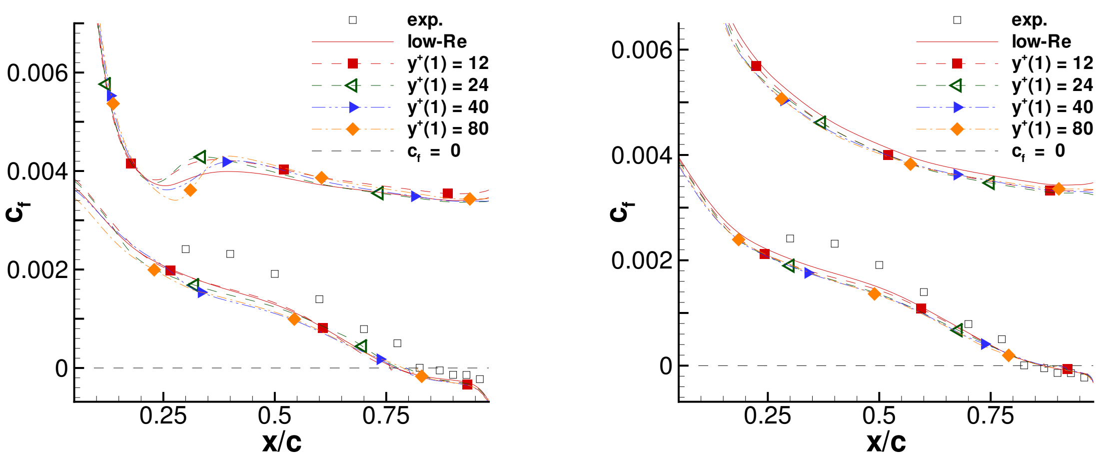

Figure 6: A-airfoil: c_{f} on grid with y^+-adaptation for SA-E model (left) and SST k-ω model (right).

4. Conclusions

A near-wall grid adaptation technique for wall-function applications to non-equilibrium flows has been presented. The method gives promising results for 2D airfoil flows. The application of the method to 3D full aircraft configurations is subject to future research.

References

[1] G. Kalitzin, G. Medic, G. Iaccarino and P. Durbin, "Near-wall behaviour of RANS turbulence models and implication for wall functions", *Journal of Computational Physics*, **2**04, 265–291 (2005).

[2] T. Knopp, T. Alrutz and D. Schwamborn, "A grid and flow adaptive wall-function method for RANS turbulence modelling", *Journal of Computational Physics* (accepted).

[3] T. Knopp, "Model-consistent universal wall-functions for RANS turbulence modelling", *Proceedings International Conference BAIL 2006, Göttingen, July 2006*, (submitted).

[4] J.R. Edwards and S. Chandra, "Comparison of eddy viscosity-transport turbulence models for three-dimensional, shock separated flowfields", *AIAA Journal*, **3**4, 756–763 (1996).

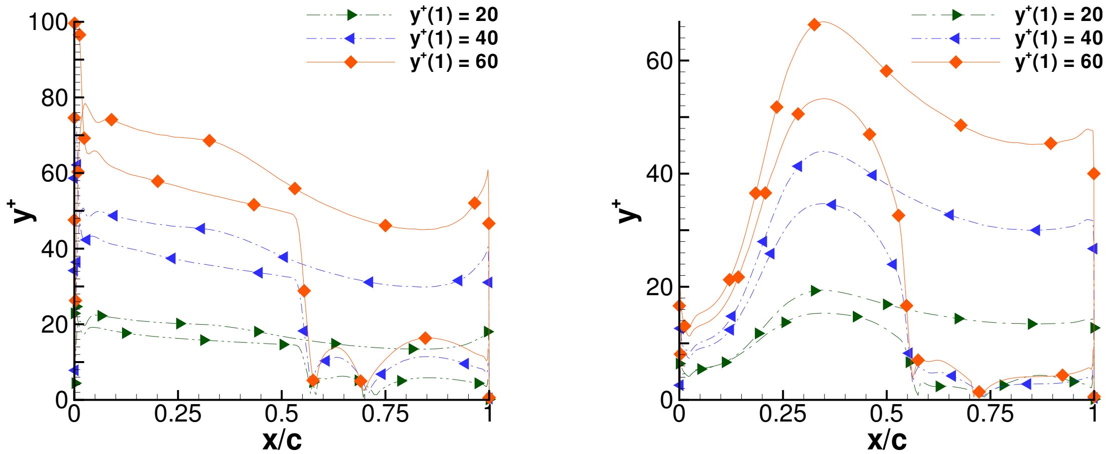

Figure 7: RAE case 10: Distribution of $y^+(1)$ for SST k-ω without (left) and with (right) y^+-adaptation.

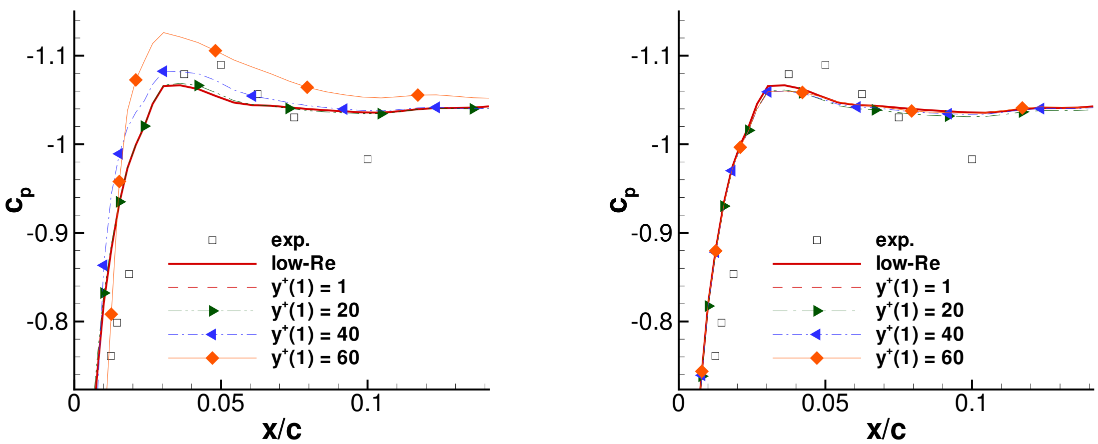

Figure 8: RAE case 10: Prediction for c_p for SA-E model without (left) and with (right) y^+ adaptation.

[5] F.R. Menter, "Zonal two equation k/ω turbulence models for aerodynamic flows", *AIAA Paper 1993-2906*, (1993).

[6] P. Aumann, H. Barnewitz, H. Schwarten, K. Becker, R. Heinrich, B. Roll, M. Galle, N. Kroll, Th. Gerhold, D. Schwamborn, M. Franke "MEGAFLOW: Parallel complete aircraft CFD", *Parallel Computing*, **2**7, 415–440 (2001).

[7] P. H. Cook, M. A. McDonald and M.C.P. Firmin, "Aerofoil RAE 2822 - Pressure distributions and boundary layer and wake measurements", *AGARD Advisory Report AR-138*, A6.1-A6.77, (1979).

[8] Ch. Gleyzes, "Opération décrochage - Résultats des essais à la soufflerie F2", *RT-DERAT 55/4004 DN, ONERA*, (1988).

[9] Ch. Gleyzes, "Opération décrochage - Résultats de la 2ème campagne d'essais à F2 – Mesures de pression et vélocimétrie laser", *RT-DERAT 55/5004 DN, ONERA*, (1989).

[10] Th. Alrutz, "Hybrid grid adaptation in TAU", *In: MEGAFLOW - Numerical flow simulation for aircraft design, Notes on Numerical Fluid Mechanics and Multidisciplinary Design. N. Kroll and J.K. Fassbender, Eds.*, (2005).

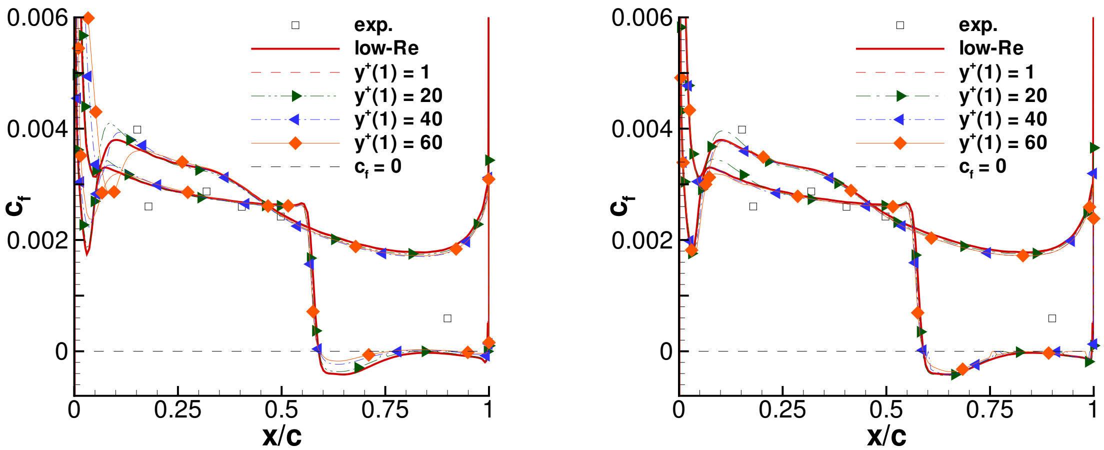

Figure 9: RAE case 10: Prediction for c_f for SA-Edwards model without (left) and with (right) y^+-adaptation.

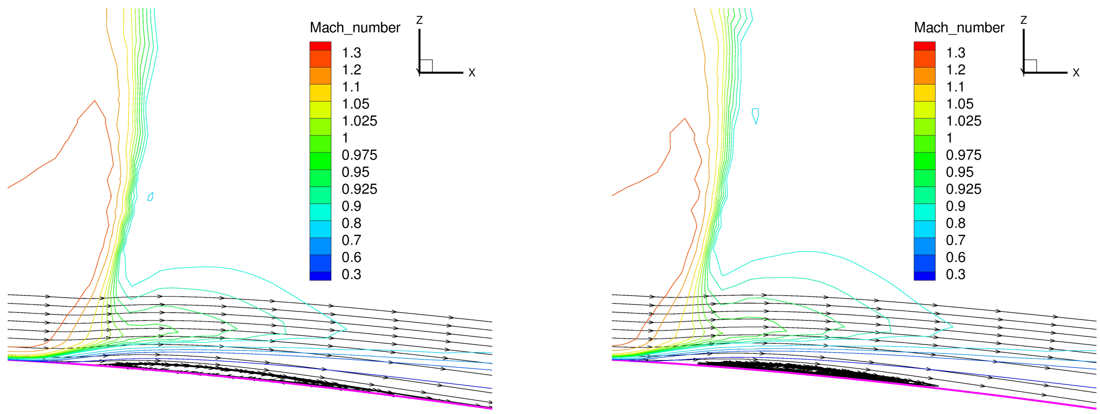

Figure 10: RAE case 10: Details of shock-pattern (Mach number isolines) and streamtraces for velocity on wall-resolved grid with $y^+(1) = 1$ (left) and on grid with $y^+(1) = 60$ with y^+-adaptation in the region of flow separation (right) for SA-E model.

[11] T.J. Baker, "Identification and Preservation of Surface Features", *Proceedings, 13th International Meshing Roundtable, Williamsburg, VA, Sandia National Laboratories, September 19-22 2004*, pp.299–310 (2004).